Journal of Vacuum Science & Technology A



# Oxidation behavior of a cathodic arc evaporated $Cr_{0.69}Ta_{0.20}B_{0.11}N$ coating

Christina Kainz[1], Ilse Letofsky-Papst[2], Christian Saringer[1,†], Hannes Krüger[3], Andreas Stark[4], Norbert Schell[4], Markus Pohler[5], Christoph Czettl[5]

[1] *Christian Doppler Laboratory for Advanced Coated Cutting Tools at the Department of Materials Science, Montanuniversität Leoben, Franz-Josef-Straße 18, 8700 Leoben, Austria*

[2] *Institute of Electron Microscopy and Nanoanalysis and Center for Electron Microscopy, Graz University of Technology, NAWI Graz, Steyrergasse 17, 8010 Graz, Austria*

[3] *Institute of Mineralogy and Petrography, University of Innsbruck, Innrain 52, 6020, Innsbruck, Austria*

[4] *Institute of Materials Physics, Helmholtz-Zentrum Hereon, Max-Planck-Straße 1, 21502 Geesthacht, Germany*

[5] *Ceratizit Austria GmbH, Metallwerk-Plansee-Straße 71, 6600 Reutte, Austria*

[†] *now with: AT&S Austria Technologie & Systemtechnik, Fabriksgasse 13, 8700 Leoben, Austria*

**Keywords:** Synchrotron radiation, transmission electron microscopy, oxidation, cathodic arc evaporation, CrTaBN

**Abstract**

CrTaBN hard coatings deposited by cathodic arc evaporation are a promising new material class for use in demanding applications, due to their high hardness and good thermal stability in protective atmosphere. Up to now however, studies on the detailed oxidation mechanism of quaternary CrTaBN coatings are lacking in literature. Thus, within this work, the oxidation behavior of a $Cr_{0.69}Ta_{0.20}B_{0.11}N$ coating grown by cathodic arc evaporation was studied in a combinatorial approach of advanced characterization techniques. *In-situ* high-energy X-ray diffraction at a synchrotron radiation facility showed that up to ~1100 °C, only the face-centered

Journal of Vacuum Science & Technology A



cubic (fcc) $Cr_xTa_yB_{1-x-y}N$ solid solution of powdered CrTaBN contributes to the crystalline phase composition. As the temperature is further increased, tetragonal $CrTaO_4$ and rhombohedral $Cr_2O_3$ form. *In-situ* high-temperature Raman spectroscopy evidenced that $B_2O_3$ contributes to the phase composition of the material in the temperature regime from ~600 to 1000 °C. Applying high-resolution transmission electron microscopy allowed to identify the presence of four discrete zones in a partly oxidized CrTaBN coating on sapphire: intact fcc-CrTaBN at the interface to the substrate, followed by a Cr-deficient and Cr-enriched layer, respectively, and a porous layer with small grains at the surface.

## I. Introduction

Ternary CrN based hard coatings are established materials for use in severe applications, such as glass molding or metal cutting. CrAlN is the industrially most important representative of CrN based ternary metal nitrides, which can be attributed to its high hardness and good oxidation resistance.[1–3] Thus, literature on CrAlN hard coatings grown by means of both, magnetron sputter deposition and cathodic arc evaporation (CAE), is vast.[2–7] In contrast, CrTaN coatings have only recently gained interest for use in demanding applications.[8–10] As was shown in previous studies by the authors, CrTaN coatings offer a combination of high hardness, beneficial fracture toughness and good tribological properties.[11,12] In contrast to metastable CrAlN,[13] CrN and TaN exhibit a negative mixing enthalpy regardless of the Cr/(Cr+Ta) ratio in the resulting face-centered cubic (fcc) $Cr_xTa_{1-x}N$ solid solution.[14] This fact is in line with the high thermal stability of CrTaN coatings up to temperatures of ~1250 °C.[11,15] In addition, CrTaN coatings exhibiting a high Cr/(Cr+Ta) ratio have been shown to offer an outstanding oxidation resistance, where the formation of the oxides only sets in at temperatures of ~1050 °C.[16,17]

The addition of B to ternary transition metal nitrides is an effective strategy to improve their mechanical and thermo-physical properties and thus, to widen their application portfolio.[18–21] Ma *et al.* reported that the hardness is increased by more than 70 % in CrBN as compared to CrN coatings.[18] Hu *et al.* have shown that the presence of already 3-6 at.% of B improves the hardness and thermal stability of CrAlN coatings.[22] The feasibility to add B to CrTaN has been confirmed in an earlier work by the authors. There, it was shown that quaternary CrTaBN outperforms CrTaN in regard of hardness and fracture toughness, which can be attributed to the grain refining effect of B. The obtained hardness of ~32 GPa furthermore not only exceeds the values reported for arc evaporated CrTaN coatings (~26 GPa),[11] but also those of arc evaporated CrBN (25.9 GPa).[23] In addition, CrTaBN was found to exhibit a high thermal stability in protective atmosphere up to temperatures of 1200 °C.[24] However, the oxidation mechanism of quaternary CrTaBN is widely unexplored, although B is reported to increase the oxidation resistance of several transition metal nitride coatings.[22,25,26]

Thus, within this work, the oxidation behavior of an arc evaporated $Cr_{0.69}Ta_{0.20}B_{0.11}N$ coating is illuminated in a combinatorial approach of advanced characterization techniques. Prior to the oxidation study, the microstructure of the as-deposited coating was investigated by lab-scale X-ray diffraction (XRD) and scanning electron microscopy (SEM). *In-situ* high-energy XRD experiments at a synchrotron radiation facility as well as *in-situ* high-temperature Raman spectroscopy allowed to study the oxidation mechanism of powdered $Cr_{0.69}Ta_{0.20}B_{0.11}N$. Differential thermal analysis (DTA) and thermo-gravimetric analysis (TGA) coupled with mass spectrometry (MS) supplemented the crystallographic and spectroscopic investigations. In addition, lab-scale high-temperature XRD was applied to illuminate the oxidation progress of the compact coating on sapphire. Finally, a partly oxidized coating was investigated by SEM, energy

dispersive X-ray spectroscopy (EDX) and transmission electron microscopy (TEM) to study the microstructure of the oxide scale.

## II. Materials and methods

The investigated CrTaBN coating was deposited in an industrial scale Oerlikon Balzers INNOVA deposition system. Four powder metallurgically produced compound targets were used to deposit the coating. The target composition amounted to 70 at.% Cr, 20 at.% Ta and 10 at.% B. The deposition runs were conducted in pure $N_2$ atmosphere at a substrate temperature of 450 °C and a bias voltage of -60 V. This bias voltage was selected based on earlier studies on arc evaporated CrTaBN[24] and CrTaN coatings.[16] A $N_2$ pressure and arc current of $3.6\times10^{-2}$ mbar and 130 A, respectively, were applied during deposition. Prior to the actual deposition, an ion etching step in pure Ar atmosphere was applied. The coatings were grown on mild steel foil and 0001 oriented sapphire substrates, which were subjected to two- and three-fold rotation, respectively. In order to obtain coating powders, the mild steel foil was dissolved after deposition using sulfuric acid.

The chemical composition of the coating on cemented carbide was quantified by glow discharge optical emission spectroscopy (GDOES) using a GD-Profiler 2 by Horiba, operating in pulsed RF mode.[27] Cross-sectional micrographs of the coating were realized by focused ion beam milling using a dual beam workstation from Zeiss. An initial assessment of the microstructure was realized by lab-scale XRD utilizing a Bruker AXS D8 Advance diffractometer, operating in Bragg-Brentano geometry and with $CuK_\alpha$ radiation. The residual stress of the coating on sapphire was determined on the same diffractometer applying the $\sin^2\psi$ method in side-inclination with parallel beam optics.[28] Using the 220 reflection, twelve equally spaced inclinations from 0-0.6 $\sin^2\psi$ were considered in the residual stress evaluation. Applying a rule of mixture between

fcc-CrN and fcc-TaN and elastic constants from ref.[29] and [30] were used to calculate stress from measured strain.

High energy XRD experiments were carried out at the high energy materials science beamline P07 of the Helmholtz-Zentrum Hereon at the PETRA III storage ring in Hamburg, Germany.[31] The powdered coating was placed in a Pt crucible and was heated to 1400 °C at a rate of 20 °C/min. The X-ray beam featured an energy of 103.2 keV, which corresponds to a wavelength of 0.11965 Å. 2D X–ray diffractograms were recorded every ~2 °C with an XRD 1621 flat–panel detector by Perkin Elmer. In order to obtain one-dimensional diffractograms, the two-dimensional Debye Scherrer rings recorded at the synchrotron radiation facility were azimuthally integrated over the whole angular range. For further details on the measurement procedure, azimuthal integration and subsequent quantitative Rietveld refinement, the reader is referred to ref.[16] Using a Tescan type Clara microscope equipped with a detector by Oxford instruments allowed to assess the chemical composition of the powder after the heat treatment in air by means of a combination of energy (EDX) and wavelength dispersive X-ray spectroscopy (WDX). Raman spectroscopy investigations were realized using a WITec alpha300R confocal Raman microscope. The power of the laser, which exhibited a wavelength of 532 nm, was defined at 10 mW. *In-situ* high-temperature experiments were realized with a heating chamber type TS1500V provided by Linkam. A maximum temperature and heating rate of 1400 °C and 20 °C/min, respectively, were chosen for the measurement. Complementary, DTA-TGA was performed on a Setaram SetsysEvolution 2400, using 72.5 mg of the sample material in a 100 µl $Al_2O_3$ crucible and an empty crucible of the same type as the reference. For evolved gas analysis, this device is coupled with a quadrupole mass spectrometer type OmniStar GSD-301 O2 (Pfeiffer) through a heated (150 °C) steel capillary transfer line. A heating rate of 5 °C/min and a maximum temperature of 1400 °C were chosen for the experiment, with a carrier gas (air) flow rate of 20 ml/min. For the quantitative evaluation of

the TGA data, a blank experiment subtraction was performed. MS data was sampled at 1 sec per mass to charge *(m/z)* value using a channel electron multiplier.

*In-situ* high-temperature XRD experiments were realized on the aforementioned lab-scale diffractometer, equipped with a heating chamber type HTK 1200 N by Anton Paar. Applying a heating rate of ~2.5 °C/min, a CrTaBN coating on sapphire substrate was heated to 1200 °C in open air and diffractograms were recorded every 25 °C. An additional coating on sapphire substrate was heated to 1000 °C at the same heating rate and was held for 15 minutes within the diffractometer in order to enable the investigation of a partly oxidized coating. The cross-sectional microstructure of the ion milled partly oxidized coating was studied on a Gemini 450 scanning electron microscope from Zeiss. In order to gain a solid understanding of the microstructure and elemental composition of the partly oxidized CrTaBN coating at nanoscale, also high-resolution scanning TEM (STEM) investigations were performed. The electron transparent lamella was prepared by focused ion beam milling using a FEI Nova200 dualbeam workstation. A FEI Titan3 G2 60–300, operated at an acceleration voltage of 300 kV, was used to record STEM micrographs. Here, the images were obtained utilizing a high angle annular dark-field (HAADF) detector. EDX and electron energy-loss spectroscopy (EELS) investigations were carried out on a monochromatic FEI Tecnai F20 microscope. The device is fitted with a Schottky field emission gun and was operated at an acceleration voltage of 200 kV. The EDX spectra were acquired with an EDAX Si(Li) detector with an ultrathin window. For EELS, the microscope is equipped with a high-resolution Gatan imaging filter. EDX as well as EELS measurements were acquired using the STEM mode of the microscope.

## III. Results and discussion

### A. Coating in as-deposited state

The coating composition as determined by GDOES amounted to 34.8 at.% Cr, 10.8 at.% Ta, 5.5 at.% B and 48.9 at.% N. Therefore, the resulting Cr/Ta/B ratio of 0.69/0.20/0.11 in the coating is similar to the one of the target (0.70/0.20/0.10) and the Cr/(Cr+Ta) ratio corresponds to 0.76. The cross-sectional microstructure of the coating on sapphire was studied by SEM and is shown in Fig. 1a. The morphology of the coating appears fine-grained, where the grains are too small to be resolved by means of SEM. Furthermore, nano-layers of varying composition are visible in the cross-sectional micrograph, which arise from the three-fold rotation the substrates were subjected to during the deposition.[32] The X-ray diffractogram of the powdered coating along with the one of CrTaBN on sapphire are shown in Fig. 1b. While the diffractogram of the powder was recorded at the synchrotron facility, the measurement of the coating on sapphire was realized by lab-scale XRD. Since the wavelength of the synchrotron radiation (~0.12 Å) varied from the one of the lab-scale XRD (1.54 Å), the d-spacing is given instead of the 2θ angle in Fig. 1b for better comparability. All reflections are located between the standard peak positions of fcc-CrN and fcc-TaN.[33,34] Consequently, B is either incorporated into the fcc-CrTaN lattice or exists as amorphous constituent in the material. Also, the combination of the B incorporation into the fcc lattice and the presence of amorphous constituents is possible. Thus, the crystalline structure is in the following referred to as fcc-$Cr_xTa_yB_{1-x-y}N$.

B. Oxidation resistance of coating powder

The temperature dependent phase evolution during oxidation of powdered CrTaBN is displayed in Fig. 2a in the form of a phase plot from 100 °C to 1400 °C. The phase plot can be divided into three temperature dependent zones, which are confined by the emergence or vanishing of crystalline phases. Up to ~1100 °C (zone 1), only reflections stemming from the fcc-$Cr_xTa_yB_{1-x-y}N$ solid solution are evident. The apparent shift to higher d-spacings with increasing temperature can be attributed to the thermal expansion of the material. At ~1100 °C (zone 2) additional reflections emerge, which can be ascribed to tetragonal (t) $CrTaO_4$,[35] followed by the formation of rhombohedral (r) $Cr_2O_3$ at ~1125 °C.[36] Both, t-$CrTaO_4$ and r-$Cr_2O_3$ are reported to form during the oxidation of ternary CrTaN coatings.[17,37] As the temperature exceeds ~1250 °C, no reflections stemming from the fcc-$Cr_xTa_yB_{1-x-y}N$ solid solution contribute to the phase plot anymore, indicating complete oxidation of the material (zone 3). According to the synchrotron investigation, crystalline BN, B-oxides or borides do not form during heating the CrTaBN powder in air up to 1400 °C. In order to gain a quantitative assessment on the temperature-dependent phase composition, a sequential Rietveld refinement was employed. At temperatures below 1050 °C the diffraction pattern did not show any distinct oxide peaks. The emergence of t-$CrTaO_4$ according to the refinement at 1075 °C corresponds well with the visual impression from the phase plot. This applies also to the slightly delayed formation of r-$Cr_2O_3$. The refinement indicates that the ratio between t-$CrTaO_4$ (~70 wt.%) and r-$Cr_2O_3$ (~30 wt.%) stays largely invariant after all of the nitride has transformed into the oxides.

Since B-containing oxides are frequently hardly detectable by means of crystallographic techniques, *in-situ* high-temperature Raman spectroscopy was applied to further elucidate the oxidation mechanism of CrTaBN. Fig. 3 shows the Raman spectra recorded at four exemplary measurement temperatures. The as-deposited coating exhibits rather broad signals, where the bands

in the wavenumber regime of 100-200 and 400-800 $cm^{-1}$ can be attributed to the acoustical (A) and optical (O) modes, respectively, of the $Cr_xTa_yB_{1-x-y}N$ solid solution.[38,39] No cubic or hexagonal BN was detected regardless of the measurement temperature. As the temperature reaches ~600 °C, a broad peak with a maximum at 800 $cm^{-1}$ emerges, which can be attributed to $B_2O_3$.[40] The $B_2O_3$ peak increases in intensity up to ~800 °C, but vanishes as the temperature exceeds 1000 °C. This observation suggests that $B_2O_3$ forms volatile species upon increasing the temperature to >1000 °C. Both, the emergence of $B_2O_3$ in the course of the oxidation of B-containing coatings as well as the formation of volatile species from this compound is in agreement with existing literature.[23,40,41] EDX/WDX measurements furthermore confirmed the absence of B in the powdered coating subjected to 1400 °C in air. Three well-defined peaks contribute to the Raman spectrum recorded at 1200 °C. Here, the peaks at ~300 and 520 $cm^{-1}$ correspond to $Cr_2O_3$.[42] Taking into account the phase composition of the coating at 1200 °C as determined by high-energy XRD (Fig. 2), it is suggested that the additional peak at ~950 $cm^{-1}$ stems from $CrTaO_4$. In order to verify this hypothesis, a Raman spectrum of an oxidized $Cr_{0.46}Ta_{0.54}N$ coating, exhibiting only the $CrTaO_4$ phase as oxidation product, was recorded.[17] Indeed, the spectrum showed a pronounced peak at ~950 $cm^{-1}$, confirming the presence of the $CrTaO_4$ phase also in the here conducted Raman experiment. Summarizing, the investigated CrTaBN powder exhibits a comparable oxidation behavior as a powdered CrTaN coating with an equivalent Cr/(Cr+Ta) ratio grown at similar deposition conditions. This fact applies both, in regard of the formed crystalline oxides and formation onset temperature of t-$CrTaO_4$ and r-$Cr_2O_3$.[16] However, X-ray amorphous $B_2O_3$ contributes to the phase composition in the temperature regime from ~600 to 1000 °C. Since $B_2O_3$ is reported to heal macro-defects and pores, its formation in the course of the oxidation of CrTaBN is suggested to be beneficial for the coating performance in service.[43] Taking into account also the

improved mechanical properties of CrTaBN as compared to CrTaN speaks for the preferred use of the quaternary coating system in demanding applications.[16,24]

DTA/TGA-MS experiments complemented the crystallographic and spectroscopic investigation of the CrTaBN oxidation. The relative mass change, DTA signal and ion current of the NO with a (*m/z*) of 30 are shown in Fig. 4a, b and c, respectively, as a function of the temperature. While there is a deviation from the baseline of the DTA-signal between ~300 to 900 °C, no major peak is evident in the TGA curve in this temperature regime. It is assumed that due to the low fraction of B in the material, the formation of $B_2O_3$ during oxidation does not provoke major events in the mass change curve. Furthermore, a superimposition of the mass gain resulting from the formation of solid oxides and mass loss stemming from the evaporation of volatile species resulting in no visible net change of the sample mass is plausible. A pronounced exothermic peak is evident between ~1000 and 1200 °C, which is ascribed to the oxidation of the fcc-$Cr_xTa_yB_{1-x-y}N$ solid solution to t-$CrTaO_4$ and r-$Cr_2O_3$. This temperature range is in good accordance with the *in-situ* oxidation study (Fig. 2) conducted at the synchrotron radiation facility. The highest mass change during the measurement was observed at a temperature of 1200 °C and amounts to 13.0 %, which is temperature-wise again in line with the synchrotron study. As the temperature is further increased, the mass decreases to 12.2 % of the initial mass at 1400 °C. This behavior indicates the formation of volatile oxides, which are commonly observed in the course of the oxidation of B-containing compounds.[41,44,45] This suggestion is supported by the fact that ternary CrTaN with a comparable Cr/(Cr+Ta) ratio does not undergo a mass loss during oxidation.[16] In order to identify volatile species forming during the oxidation of CrTaBN, mass spectra were recorded in the course of the experiment. In Fig. 4, the ion current of *m/z* 30 is shown, which is suggested to correspond to NO. The maximum of this spectrum is observed at a temperature of ~1180 °C, which is in good agreement with the peak temperature of the DTA

measurement. Furthermore, also $NO_2$ (*m/z* 46) was detected in this temperature regime. The N-containing oxides form in the course of the CrTaBN oxidation as a result of the evaporation of $N_2$. In contrast to NO and $NO_2$, no B-containing volatile species could be detected. It is proposed that this can be attributed to the used measurement set-up: during the transport of the gaseous species from the crucible to the mass spectrometer, they have to pass a cooler regime (the furnace bottom flange and transfer line are heated to 150 °C). Species that do not exist in a gaseous state at this temperature condensate or resublimate within this transfer zone and thus are not detectable.

C. Oxidation resistance of coating on sapphire

In order to investigate the oxidation resistance of an intact coating, CrTaBN on sapphire was subjected to a heat treatment in air, where the X-ray diffractograms were simultaneously recorded. Since the used high temperature stage can only be operated up to 1200 °C, the measurement was performed in a temperature range from RT to 1200 °C. The resulting phase plot is shown in Fig. 5a. As for the powdered coating, t-$CrTaO_4$ and r-$Cr_2O_3$ form during the oxidation of CrTaBN on sapphire. Here, the oxidation onset temperature of ~900 °C is by ~200 °C lower in comparison to the one of the powdered coating as determined in the synchrotron experiment. The lower oxidation onset temperature of the intact coating can be attributed to the significantly lower heating rate used for the lab-scale XRD investigation (~2.5 °C/min) as compared to the synchrotron study (20 °C/min).

To better understand local elemental and structural changes occurring during oxidation, a partially oxidized CrTaBN coating on sapphire was studied in detail across the coating thickness. Fig. 5b shows a cross-sectional micrograph of the partially oxidized CrTaBN coating, where several different layers can be identified: the bottom ~1.5 µm thick zone exhibits a comparable microstructure as the one of the coating in the as-deposited state (Fig. 1a). Thus, this zone consists

of fcc-$Cr_xTa_yB_{1-x-y}N$. At the coating surface, a ~0.8 µm thick zone is evident, with alternating porous and dense layers. This region can be attributed to the oxide scale and exhibits a comparable morphology as the one observed in a ternary partly oxidized CrTaN coating.[16]

A lamella of the partly oxidized CrTaBN sample was investigated by STEM in order to further assess the microstructure and phase composition within the respective zones. The HAADF micrograph in Fig. 6a gives an overview of the microstructure in the respective zone. Within the substrate near zone, the EDX elemental maps indicate a homogenous distribution of Cr, Ta and N. Furthermore, no O was detected in this zone, neither within the grains nor at the grain boundaries. As already assumed from the cross-sectional SEM micrograph in Fig. 5b, the oxide scale consists of different zones with varying porosity and elemental composition. The porous layer directly on top of the non-oxidized zone is, in comparison to the intact CrTaBN layer, rich in Ta and deficient in Cr. A drastically decreased amount of N can be detected within this zone, which has been replaced by O. The subsequent layer, which is rich in Cr, exhibits a significantly denser microstructure as compared to the other layers within the oxide scale. Finally, the outermost Ta-rich layer displays again a high degree of porosity. Several publications show that a layered oxide scale forms upon oxidizing ternary or quaternary CrN-based coatings. In an earlier work, the authors observed that only $Cr_2O_3$ can be detected at the surface of a partly oxidized CrTaN coating, whereas both, $CrTaO_4$ and $Cr_2O_3$ contribute to the phase composition in an intermediate zone.[16] Similarly, Hu *et al.* observed that in case of CrAlN and CrAlBN coatings, an outermost Cr-rich oxide layer forms, followed by an Al-rich oxide layer at the interface to the non-oxidized nitride.[22]

EELS (Fig. 6b) allowed to draw further conclusions on the chemical composition within the coating in non-oxidized and oxidized state. In the latter case, the spectrum was recorded within the outermost porous Ta-rich layer. Both, the shape and position of the Cr $L_{2,3}$ edge within the non-oxidized zone are in good agreement with a spectrum recorded on a CrN coating by Kormout

*et al.*[46]. The Cr $L_{2,3}$ edge from the outermost Ta-rich oxide layer exhibits a higher accordance with the spectrum reported for $CrTaO_4$ [47] than for $Cr_2O_3$.[48] While there are some minor indications for O according to EELS in the non-oxidized zone, a pronounced signal is evident for this element in the oxidized zone. Again, a better agreement with the O K edge of $CrTaO_4$ [47] than with the one of $Cr_2O_3$ is evident.[48] Distinct signals from the N K edge contribute to the spectrum recorded within the non-oxidized zone, which is not the case for the oxidized zone. The insert in Fig. 6b shows the electron energy loss near edge fine structure of the B K edge. Owing to the low content of B within the coating, detailed statements on the chemical bonding are not possible. It can, however, be seen that the signal recorded within the non-oxidized layer is more pronounced as compared to the oxidized layer. This observation indicates a lower B content within the oxide scale as compared to the intact CrTaBN layer. In addition to the minor mass loss between 1200 and 1400 °C (Fig. 4) and the disappearance of the $B_2O_3$ signal in the Raman measurement after 1000 °C (Fig. 3) this further corroborates the formation of volatile B-containing species during the oxidation of CrTaBN.

The ADF micrograph in Fig. 7a shows the intact CrTaBN layer and the oxide scale. Based on the elemental composition, as determined from the EDX elemental maps in Fig. 6a and the grain size, four different zones can be differentiated. In order to clarify the phase composition in the respective zones, high-resolution STEM micrographs were recorded and subsequently investigated by means of Fast-Fourier-Transformation (FFT). The results of this investigation are summarized in Fig. 7b. Within the intact CrTaBN zone, only d-spacings corresponding to the fcc-$Cr_xTa_yB_{1-x-y}N$ solid solution could be detected, as for instance 2.4 Å. Within zone 2, grains with d-spacings of 3.6 Å and 3.3 Å were identified, which can be attributed to the 012 plane of r-$Cr_2O_3$ and the 110 plane of t-$CrTaO_4$, respectively. Thus, both r-$Cr_2O_3$ and t-$CrTaO_4$ contribute to the phase composition of this zone. In contrast, no indications for the t-$CrTaO_4$ phase were observed in the dense Cr-rich zone 3. Therefore, this zone seems to consist entirely of r-$Cr_2O_3$. Within the

outermost zone 4, again lattice spacings of both, r-$Cr_2O_3$ and t-$CrTaO_4$ were detected. The phase composition within the respective zone seems to not only influence the elemental composition (compare Fig. 6a), but also the local grain size. The grain size is small in case of the intact CrTaBN (zone 1), which can be attributed to the grain refining effect of B. It furthermore appears that the presence of t-$CrTaO_4$ (zone 2 and 4) results in a larger grain size as compared to zone 3, where only r-$Cr_2O_3$ was detected. Zone 3 furthermore appears significantly denser as compared to zone 2 and 4. This observation is in agreement to earlier oxidation studies on CrN based coatings, where the formed $Cr_2O_3$ oxide scale is reported to exhibit a dense structure.[1,22,49]

## IV. Conclusions

Within this work, the oxidation resistance of a quaternary $Cr_{0.69}Ta_{0.20}B_{0.11}N$ coating grown by cathodic arc evaporation was investigated, employing a variety of advanced characterization methods. *In-situ* high-energy X-ray diffraction at a synchrotron radiation facility confirmed a high oxidation resistance of the powdered coating: the crystalline fcc-$Cr_xTa_yB_{1-x-y}N$ solid solution starts to oxidize to t-$CrTaO_4$ and r-$Cr_2O_3$ only as the temperature exceeds ~1100 °C when heated at 20 °C/min. *In-situ* high-temperature Raman spectroscopy evidenced that $B_2O_3$ furthermore contributes to the phase composition between ~600 and 1000 °C. A cross-sectional investigation of CrTaBN on sapphire heated to 1000 °C at 2.5 °C/min allowed insight into the structure of a partly oxidized coating. Here, three different layers were identified within the oxide scale: a porous Cr- and Ta-containing layer at the interface to the non-oxidized CrTaBN, a dense Cr-rich intermediate layer and again a Ta-rich porous layer at the surface. The findings from the present study confirm the outstanding oxidation resistance of CrTaBN and provide a solid understanding of the oxidation sequence of this coating system.

**Acknowledgements**

The financial support by the Austrian Federal Ministry for Digital and Economic Affairs and the National Foundation for Research, Technology and Development is gratefully acknowledged. We thank Dr. Jarosław Wosik (Materials Center Leoben) and Dr. Julian Wagner (Materials Center Leoben) for SEM/FIB/EDX work. The authors acknowledge DESY (Hamburg, Germany), a member of the Helmholtz-Zentrum Hereon, for the provision of experimental facilities.

**Data availability statement**

Data available on request from the authors.

**Author declarations**

Conflict of interest

The authors have no conflicts to disclose.

**References**

[1] Y. C. Chim, X. Z. Ding, X. T. Zeng, and S. Zhang, Thin Solid Films **517,** 4845 (2009).

[2] H. Willmann, P. H. Mayrhofer, L. Hultman, and C. Mitterer, Int. Heat Treat. Surf. Eng. **1,** 75 (2007).

[3] H. Willmann, P. H. Mayrhofer, P.O.Å. Persson, A. E. Reiter, L. Hultman, and C. Mitterer, Scripta Mater. **54,** 1847 (2006).

[4] P. H. Mayrhofer, H. Willmann, and A. E. Reiter, Surf. Coat. Technol. **202,** 4935 (2008).

[5] A. Drnovšek, M. Rebelo de Figueiredo, H. Vo, A. Xia, S. J. Vachhani, S. Kolozsvári, P. Hosemann, and R. Franz, Surf. Coat. Technol. **372,** 361 (2019).

[6] N. Jäger, S. Klima, H. Hruby, J. Julin, M. Burghammer, J. F. Keckes, C. Mitterer, and R. Daniel, Acta Mater. **162,** 55 (2019).

[7] C. Sabitzer, J. Paulitsch, S. Kolozsvári, R. Rachbauer, and P. H. Mayrhofer, Thin Solid Films **610,** 26 (2016).

[8] Y.-I. Chen, Y.-T. Lin, L.-C. Chang, and J.-W. Lee, Surf. Coat. Technol. **206,** 1640 (2011).

[9] Y.-I. Chen, K.-Y. Lin, and C.-C. Chou, Thin Solid Films **544,** 606 (2013).

[10] Y.-I. Chen, K.-Y. Lin, H.-H. Wang, and K.-C. Lin, Surf. Coat. Technol. **259,** 159 (2014).

[11] C. Kainz, M. Pohler, G. C. Gruber, M. Tkadletz, A. S. Ebner, C. Czettl, and N. Schalk, Surf. Coat. Technol. **417,** 127212 (2021).

[12] N. Schalk, M. Pohler, S. Hirn, V. T. Terziyska, P. Polcik, S. Kolozsvári, C. Mitterer, and C. Czettl, Int. J. Refract. Met. Hard Mater. **71,** 211 (2018).

[13] Y. Makino, Surf. Coat. Technol. **193,** 185 (2005).

[14] L. Zhou, D. Holec, and P. H. Mayrhofer, J. Phys. D: Appl. Phys. **46,** 365301 (2013).

[15] C. Kainz, M. Tkadletz, A. Stark, N. Schell, C. Czettl, M. Pohler, and N. Schalk, Materialia **22,** 101434 (2022).

[16] C. Kainz, C. Saringer, M. Burtscher, M. Tkadletz, A. Stark, N. Schell, M. Pohler, C. Czettl, D. Kiener, and N. Schalk, Scripta Mater. **211,** 114492 (2022).

[17] C. Kainz, L. Kölbl, and N. Schalk, Surf. Coat. Technol. **447,** 128877 (2022).

[18] Q. Ma, F. Zhou, S. Gao, Z. Wu, Q. Wang, K. Chen, Z. Zhou, and L. K.-Y. Li, Appl. Surf. Sci. **377,** 394 (2016).

[19] Q. Wang, F. Zhou, Z. Zhou, L. K.-Y. Li, and J. Yan, Vacuum **145,** 186 (2017).

[20] C. Kainz, N. Schalk, M. Tkadletz, C. Saringer, M. Winkler, A. Stark, N. Schell, J. Julin, and C. Czettl, Surf. Coat. Technol. **384,** 125318 (2020).

[21] C. Kainz, N. Schalk, M. Tkadletz, C. Mitterer, and C. Czettl, Thin Solid Films **688,** 137283 (2019).

[22] C. Hu, L. Chen, and V. Moraes, Surf. Coat. Technol. **417,** 127191 (2021).

[23] W. Chen, T. Hu, Y. Hong, D. Zhang, and X. Meng, Surf. Coat. Technol. **404,** 126429 (2020).

[24] C. Kainz, M. Pohler, M. Tkadletz, C. Czettl, and N. Schalk, Surf. Coat. Technol. **428,** 127867 (2021).

[25] M. Nose, W.-A. Chiou, T. Kawabata, Y. Hatano, and K. Matsuda, Thin Solid Films **523,** 6 (2012).

[26] J. Zhou, C. Hu, J. Zhang, L. Chen, and Y. Kong, Int. J. Refract. Met. Hard Mater. **98,** 105531 (2021).

[27] ISO. ISO Standard 14707:2021, Surface Chemical Analysis — Glow Discharge Optical Emission Spectrometry (GD-OES) — Introduction to Use, International Organization for Standardization, Geneva, Switzerland, 2021. (2021).

[28] G. Abadias, E. Chason, J. Keckes, M. Sebastiani, G. B. Thompson, E. Barthel, G. L. Doll, C. E. Murray, C. H. Stoessel, and L. Martinu, Journal of Vacuum Science & Technology A: Vacuum, Surfaces, and Films **36,** 20801 (2018).

[29] J. Chang, G.-P. Zhao, X.-L. Zhou, K. Liu, and L.-Y. Lu, J. Appl. Phys. **112, 083519** (2012).

[30] G. C. A. M. Janssen, F. D. Tichelaar, and C. C. G. Visser, J. Appl. Phys. **100,** 93512 (2006).

[31] N. Schell, A. King, F. Beckmann, T. Fischer, M. Müller, and A. Schreyer, MSF **772,** 57 (2013).

[32] J. Sjölén, L. Karlsson, S. Braun, R. Murdey, A. Hörling, and L. Hultman, Surf. Coat. Technol. **201,** 6392 (2007).

[33] M. Widenmeyer, E. Meissner, A. Senyshyn, and R. Niewa, Z. Anorg. Allg. Chem. **640, 2801** (2014).

[34] T. Mashimo, S. Tashiro, T. Toya, M. Nishida, H. Yamazaki, S. Yamaya, K. Oh-ishi, and Y. Syono, J. Mater. Sci. **28,** 3439 (1993).

[35] W. Wong-Ng, H. F. McMurdie, B. Paretzkin, C. R. Hubbard, and A. Dragoo. Powder Diffraction. 3rd ed. (1988).

[36] H. E. Swanson, H. F. McMurdie, M. C. Morris, and E. H. Evans. Standard X-ray Diffraction Powder Patterns. 25th ed. (1955).

[37] Y.-I. Chen, B.-L. Lin, Y.-C. Kuo, J.-C. Huang, L.-C. Chang, and Y.-T. Lin, Appl. Surf. Sci. **257,** 6741 (2011).

[38] H. C. Barshilia, and K. S. Rajam, J. Mater. Res. **19,** 3196 (2004).

[39] G. B. Gaitán, A. M. E. García, A. C. Q. Ossa, and J. A. O. Vélez, Rev.EIA.Esc.Ing.Antioq **13,** 69 (2016).

[40] I. Dreiling, C. Raisch, J. Glaser, D. Stiens, and T. Chassé, Surf. Coat. Technol. **206,** 479 (2011).

[41] T. Glechner, H. G. Oemer, T. Wojcik, M. Weiss, A. Limbeck, J. Ramm, P. Polcik, and H. Riedl, Surf. Coat. Technol. **434,** 128178 (2022).

[42] Q. Li, Y. Gou, T.-G. Wang, T. Gu, Q. Yu, and L. Wang, Coatings **9,** 500 (2019).

[43] R. F. Voitovich, and É.A. Pugach, Poroshk. Metall. **2,** 57 (1975).

[44] P. H. Mayrhofer, C. Mitterer, J. G. Wen, I. Petrov, and J. E. Greene, J. Appl. Phys. **100** (2006).

[45] D. P. Gruber, J. Zalesak, J. Todt, M. Tkadletz, B. Sartory, J.-P. Suuronen, T. Ziegelwanger, C. Czettl, C. Mitterer, and J. Keckes, Surf. Coat. Technol. **399,** 126181 (2020).

[46] Kormout, K. Characterization of CrN films on MgO by Transmission Electron Microscopy. *Diploma thesis* (2012).

[47] A. M. Arevalo-Lopez, E. Castillo-Martinez, and M. Á. Alario-Franco, Mater. Res. Soc. Symp. Proc. **1148,** 31 (2008).

[48] C. Mitterbauer, G. Kothleitner, W. Grogger, H. Zandbergen, B. Freitag, P. Tiemeijer, and F. Hofer, Ultramicroscopy **96,** 469 (2003).

[49] T. Polcar, and A. Cavaleiro, Mater. Chem. Phys. **129,** 195 (2011).

**Figure captions**

*Fig. 1: a) Cross-sectional micrograph of as-deposited CrTaBN on sapphire. b) X-ray diffractogram of powdered CrTaBN and the CrTaBN coating on sapphire.*

*Fig. 2: a) XRD phase plot showing the oxidation of the CrTaBN powder. The peak positions of fcc-$Cr_xTa_yB_{1-x-y}N$ (grey triangle), t-$CrTaO_4$ (red rectangle) and r-$Cr_2O_3$ (blue circle) at room temperature (RT) are given as well. b) A sequential Rietveld refinement allowed to quantify the phase composition at every measurement temperature.*

*Fig. 3: Raman spectra of powdered CrTaBN recorded at RT, 600, 850 and 1200 °C. The Raman shift of acoustical (A) and optical (O) modes of CrTaN as well as the shifts as reported in literature for $Cr_2O_3$, $B_2O_3$ and $CrTaO_4$ are depicted.* [38–40, 42]

*Fig. 4: a) Mass change, b) heat flow and c) mass spectrum with m/z 30 recorded during heating CrTaBN powder in ambient atmosphere.*

*Fig. 5: a) Oxidation sequence of CrTaBN on sapphire as determined by lab-scale in-situ high-temperature XRD. b) Cross-sectional micrograph of a partly oxidized CrTaBN coating on sapphire. The sample has been heated at 2.5 °C/min to 1000 °C with a holding time of 15 minutes at the maximum temperature.*

*Fig. 6: a) HAADF micrograph and corresponding Cr, Ta, N and O EDX elemental maps recorded on the partly oxidized coating during the STEM analysis. A heating rate and maximum temperature of 2.5 °C/min and 1000 °C, respectively, have been applied to the coating. The black cross and red triangle mark the positions, where the spectra shown in b) have been recorded. b) EELS spectra*

*of the N K, O K and Cr $L_{2,3}$ edge recorded within the non-oxidized and oxidized zone. Within the insert, the B K edge is shown.*

*Fig. 7: a) ADF micrograph of the partly oxidized CrTaBN coating on sapphire, depicting the 4 different zones. The coating has been subjected to a maximum temperature of 1000 °C applying a heating rate of 2.5 °C/min. b) High-resolution HAADF micrograph recorded within the respective zones. The colored boxes mark the area from where the FFT images have been obtained.*

Journal of Vacuum Science & Technology A


PLEASE CITE THIS ARTICLE AS DOI: 10.1116/6.0002356

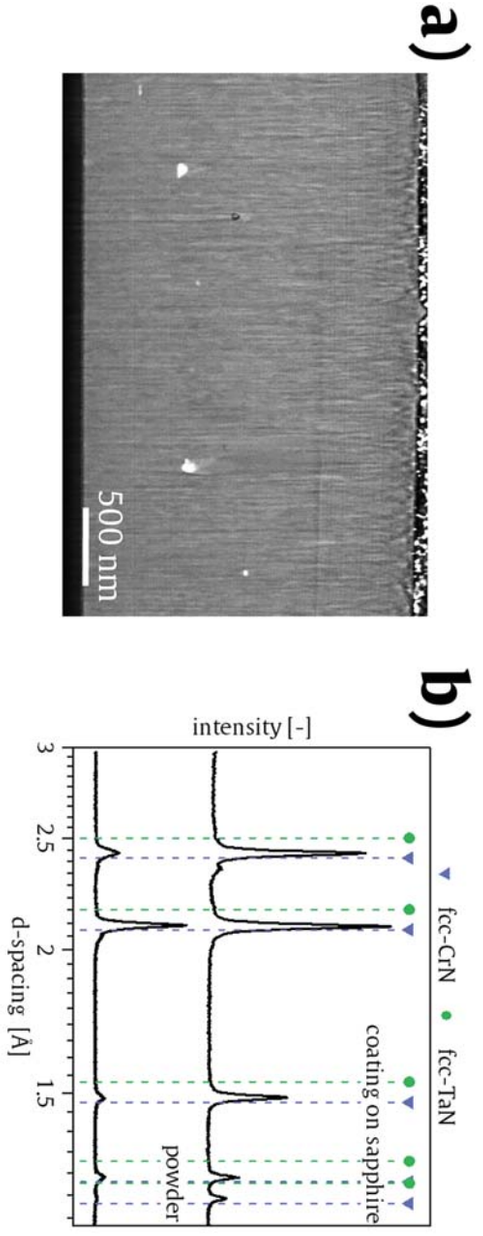

Journal of Vacuum Science & Technology A


PLEASE CITE THIS ARTICLE AS DOI: 10.1116/6.0002356

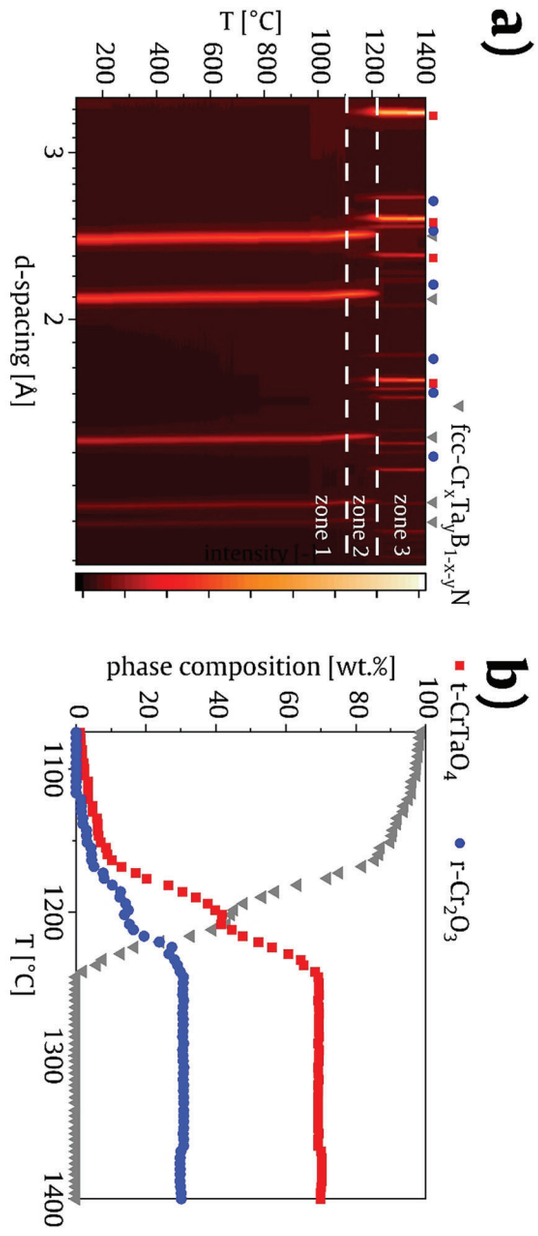

Journal of Vacuum Science & Technology A


PLEASE CITE THIS ARTICLE AS DOI: 10.1116/6.0002356

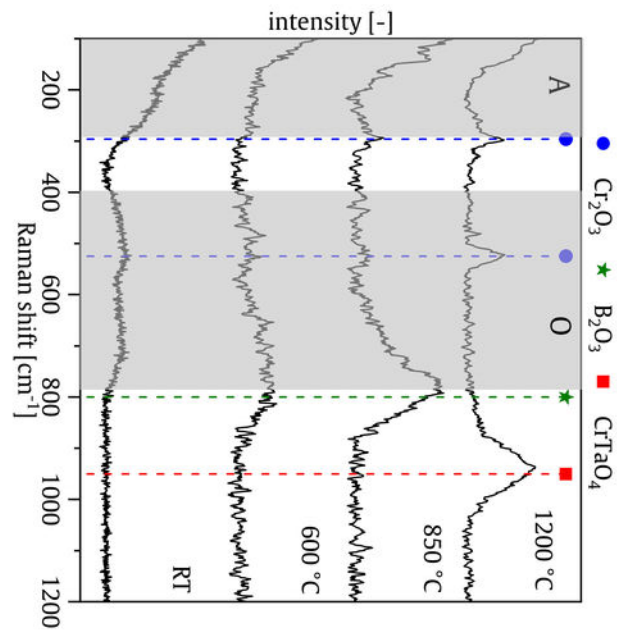

Journal of Vacuum Science & Technology A


PLEASE CITE THIS ARTICLE AS DOI: 10.1116/6.0002356

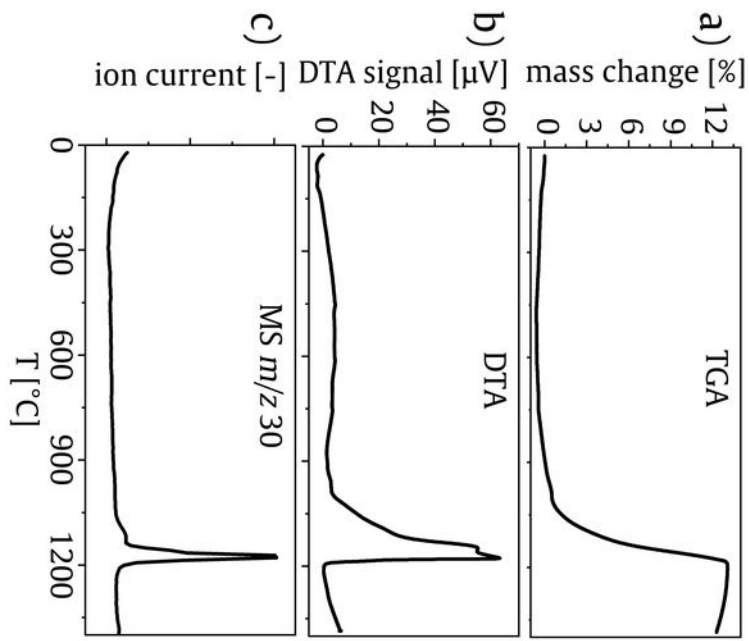

Journal of Vacuum Science & Technology A